Monotonic and cyclic lateral loading of piles in low- to medium-density chalk

R. A. McADAM*, R. M. BUCKLEY†, F. SCHRANZ‡, B. W. BYRNE§, R. J. JARDINE‖, S. KONTOE¶, T. LIU**, K. VINCK†† and J. J. CRISPIN‡‡

Offshore and other structures often rely on driven piles to carry lateral loads. However, there is currently no established design method to cover lateral loading at chalk sites, which are widespread across Northwest Europe. This paper reports monotonic and cyclic lateral load tests on highly instrumented 508 mm and 1220 mm diameter. open steel piles driven at a well-characterised chalk test site in Kent, UK, for a recent joint industry project that developed new benchmark datasets and analyses, supported by high-quality testing. The ultimate lateral pressures mobilised in the chalk are shown to be relatively low compared to its uniaxial compressive strengths (UCS) due to pile-driving damage, natural fracturing, local yielding and brittleness. Significant gaps opened between the piles and chalk during loading, that led to a substantially softer response on unloading and subsequent reloading, as well as marked axial capacity losses. Reaction curves extracted from the field measurements and applied in a one-dimensional numerical model perform well in reproducing the monotonic lateral tests. As with piles driven in other materials, one-way cyclic lateral loading led to permanent displacement accumulation and stiffness changes that were linked to the cyclic loading parameters. Both effects were more marked under biaxial cyclic lateral loading.

KEYWORDS: chalk; cyclic loading; field testing; lateral loading; pile foundations

INTRODUCTION

Many structures rely on large driven steel piles to resist cyclic and monotonic axial, lateral and moment loading, including offshore wind turbines (OWTs) that sustain critical wind and wave forces. Design often considers lateral and moment loading with '*p–y*' (e.g. API, 2014) beam–column approaches, where *p* is the soil reaction developed by a series of independent non-linear springs acting against the pile and *y* is the associated lateral displacement. North Sea jacket structure monitoring shows that the 'standard' API approach can greatly over-predict field movements offshore; see, for example, Jardine & Potts (1993) and Potts & Zdravković (2000). Instrumented field testing for the pile soil analysis project (PISA) (Byrne *et al.*, 2017) confirmed that the approach is also unsatisfactory for large-diameter monopiles in clays and sands and led to an elaboration that captured additional contributions due to distributed shaft shear tractions, base shear tractions and base pressures. The PISA reaction curves were derived from advanced three-dimensional (3D) non-linear finite-element method (FEM) analyses (Taborda *et al.*, 2020; Zdravković *et al.*, 2020) that captured soil behaviour accurately over a wide range of strains.

In this paper, piles driven in low-to-medium density chalk are considered; these are encountered widely across Northwest Europe and under the North Sea and Baltic Sea (Clayton Matthews & Heymann, 2003). No recognised code is available, and there are only two isolated case studies, to guide lateral or moment loading design in chalk. Lord & Davies (1979) describe an 800 mm dia. tubular steel pile driven to 4 m at Brighton Marina and subjected to rapid lateral loading. Ciavaglia *et al.* (2017) conducted monotonic and cyclic lateral tests at the St. Nicholas-at-Wade (SNW) test site on 762 mm dia., open tubular piles driven to approximately 4 m and 10 m. These piles included substantial angular channels used to protect the pile's strain gauges in the direction of loading, which may have influenced the resulting lateral load response.

The ALPACA (axial lateral pile analysis for chalk applying multi-scale field and laboratory testing) multi-stage joint industry project (JIP) described by Jardine *et al.* (2023) addressed the current lack of knowledge through comprehensive monotonic and cyclic pile testing, aiming to understand the underlying mechanisms and support the development of new design procedures. Jardine *et al.* (2019) and Vinck *et al.* (2022) summarise the SNW pile testing

Manuscript received 4 December 2023; revised manuscript accepted 31 July 2024. First published online ahead of print 23 August 2024.

* Formerly Department of Engineering Science, Oxford University, Oxford, UK; now Ørsted Power (UK) Ltd, London, UK (Orcid:0000-0003-0292-3549).
† James Watt School of Engineering, University of Glasgow, Glasgow, UK (Orcid:0000-0001-5152-7759).
‡ Formerly Department of Engineering Science, Oxford University, Oxford, UK; now Office of Tyrolean Regional Government, Innsbruck, Austria.
§ Department of Engineering Science, Oxford University, Oxford, UK (Orcid:0000-0002-9704-0767).
‖ Department of Civil and Environmental Engineering, Imperial College London, London, UK (Orcid:0000-0001-7147-5909).
¶ Department of Civil Engineering, University of Patras, Rio, Greece; Visiting Reader Imperial College London, London, UK (Orcid:0000-0002-8354-8762).
** Formerly Department of Civil and Environmental Engineering, Imperial College London, London, UK; now Department of Civil Engineering, University of Bristol, Bristol, UK (Orcid:0000-0002-5719-8420).
†† Department of Civil and Environmental Engineering, Imperial College London, London, UK (Orcid:0000-0002-0990-0895).
‡‡ Department of Engineering Science, Oxford University, Oxford, UK (Orcid:0000-0003-3074-8493).

programmes supported by advanced site characterisation. The linked ALPHA project (Pedone *et al.*, 2023) applied advanced 3D FEM analysis that, in a comparable way to the PISA programme, informed the field test interpretation, offering representative numerical modelling routes for practical design. Pedone *et al.* (2023) showed that the key to capturing the field response is recognizing: (*a*) the brittle, anisotropic and pressure-dependent behaviour of the chalk, as explored by Vinck *et al.* (2022) and Liu *et al.* (2022a); (*b*) the impact of driving-induced de-structuration to 'putty' and additional fracturing on stiffness and shear strength in relatively narrow annular regions around the pile shafts (see Buckley *et al.* (2018)); and (*c*) the effects of natural micro- to meso-fracturing on the stiffness of the surrounding undisturbed chalk.

High-quality, carefully instrumented field experiments in well-characterised strata provide the only reliable means of testing hypotheses of how loading style, combined with pile geometry, installation and age, affect the lateral loading response of open steel piles driven in chalk. This paper reports the lateral loading behaviour of 17 open-ended strain-gauged tubular steel piles, covering three lengths, two diameters and a wide range of monotonic and cyclic (uniaxial and biaxial) loading cases. The field work was fully successful; evaluation and interpretation of the obtained benchmark dataset allowed soil reaction models to be derived and provide evidence for future monotonic and cyclic design framework validation. An outline of the testing arrangements is given first, including the instrumentation and data acquisition and handling arrangements. The experimental programme and main results are set out, before describing how (*a*) soil reaction curves were extracted directly from the field data and (*b*) the cyclic test outcomes relate to the normalised loading parameters. Discussion follows as to how the backbone monotonic loading curves relate to cyclic tests and the chalk properties, taking insights from the ALPHA project's 3D FEM analyses (Pedone *et al.*, 2023).

TEST SITE

The SNW test site is located southwest of Margate, Kent, UK, where largely unweathered, low-to medium-density structured grade B3–A2 (Bowden *et al.*, 2002) chalk is encountered from the ground surface. Vinck *et al.* (2022) describe the site characterisation including multiple piezocone penetrations (CPTu) and seismic cone penetration test (SCPT) soundings, Geobore-S boreholes, high-quality block sampling and pressure-meter testing. The water table is located at approximately 6 m depth and CPT q_t values fall predominantly between 10 and 20 MPa over the pile lengths. Over 80 locally instrumented triaxial stress path tests were conducted under monotonic and cyclic conditions (Ahmadi-Naghadeh *et al.*, 2022; Liu *et al.*, 2022b). The chalk is markedly brittle when sheared from in situ stress conditions, giving similar peak deviator stresses, q_{max}, in drained and undrained triaxial compression tests between 1·9 and 3·3 MPa, with a 2·65 MPa mean. The in situ shear stiffnesses, G_{vh}, interpreted from SCPTs, show a mean ≈ 1·6 GPa over the depth range of interest and a trend to increase with depth. However, the maximum stiffness that could be mobilised in the SNW chalk mass by foundation loading was found by Jardine *et al.* (2023) and Pedone *et al.* (2023) to be several times lower than implied by field geophysical profiling, or locally instrumented laboratory tests. Matthews & Clayton (2004) attributed this behaviour to the chalk's systems of micro- to macro-fissuring.

PILE DETAILS

The piles were tested between July 2018 and November 2021. The pile layout and other details are summarised in Fig. 1 and Table 1. Pile name and test number conventions correspond with those presented in Jardine *et al.* (2023). The geometries employed a range of diameters and wall thicknesses including:

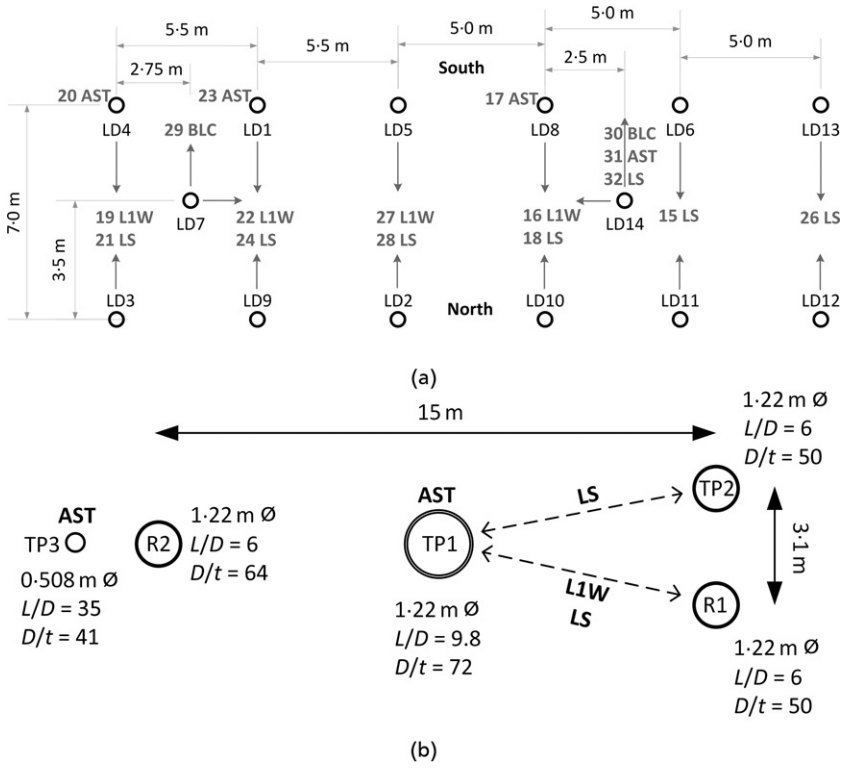

Fig. 1. Plan of pile installation layout for (a) Ø508 mm *L/D* = 6 to 20 test piles and (b) Ø1.22 m *L/D* = 6 test piles, with labels showing test order (LS = lateral monotonic; L1W = lateral uniaxial one-way cyclic; AST = axial static tension post L1W; BLC = biaxial lateral cyclic).

Table 1. Test pile geometries for pile testing under lateral monotonic, lateral cyclic and post lateral cyclic axial loading. (LS, lateral monotonic; L1W, lateral uniaxial one-way cyclic; AST, axial static tension post L1W; BLC, biaxial lateral cyclic). Age is defined as the number of days from installation to test

Test	Date tested	Age: days	Pile	D: m	L/D	D/t	Ground: mAOD	h*: m	Type	Notes
15	11/8/18	262	LD06 vs LD11	0·508	20	25	6·54/6·52	0·83/0·81	LS	First-time lateral monotonic
16	14/8/28	266	LD08 vs LD10	0·508	20	25	6·53/6·53	0·86/0·87	L1W	Lateral one-way cyclic
17	16/8/18	268	LD08	0·508	20	25	6·53		AST	Test axial capacity post L1W
18	20/8/18	272	LD08 vs LD10	0·508	20	25	6·53/6·53	0·78/0·87	LS	Test lateral capacity post L1W
19	22/8/18	273	LD03 vs LD04	0·508	20	25	6·52/6·62	0·82/0·81	L1W	Lateral one-way cyclic
20	23/8/18	275	LD04	0·508	20	25	6·62		AST	Test axial capacity post L1W
21	05/9/18	287	LD03 vs LD04	0·508	20	25	6·52/6·62	0·84/0·85	LS	Test lateral capacity post L1W
22	07/9/18	289	LD01 vs LD09	0·508	20	25	6·92/6·64	0·95/0·94	L1W	Lateral one-way cyclic
23	08/9/18	290	LD01	0·508	20	25	6·92		AST	Test axial capacity post L1W
24†	10/9/18	292	LD01 vs LD09	0·508	20	25	6·92/6·64	1·00/0·96	LS	Test lateral capacity post L1W
26	12/9/18	295	LD12 vs LD13	0·508	6	25	6·56/6·49	0·96/0·95	LS	First-time lateral monotonic
27	19/9/18	302	LD02 vs LD05	0·508	20	25	6·54/6·54	0·96/0·97	L1W	Ended early – load cell failure
28	21/9/18	304	LD02 vs LD05	0·508	20	25	6·54/6·54	0·97/0·98	LS	Test lateral capacity post L1W
29	24/9/18	307	LD07	0·508	20	25	6·56	0·92/0·95	BLC	Practice biaxial lateral cyclic
30	26/9/18	134	LD14	0·508	20	25	6·50	1·07/1·08	BLC	Biaxial lateral cyclic
31	28/9/18	136	LD14	0·508	20	25	6·50		AST	Test axial capacity post BLC
32	02/10/18	140	LD14	0·508	20	25	6·50	1·05	LS	Test LS capacity post BLC
+3	18/11/21	406	TP2 vs TP1	1·22/ 1·8	6	50/ 72	6·50/6·44	0·94/1·08	LS	First-time lateral monotonic
+4	25/11/21	415	R1 vs TP1	1·22/ 1·8	6	50/ 72	6·48/6·44	0·98/1·05	L1W	Lateral one-way cyclic
+5	26/11/21	416	R1 vs TP1	1·22/ 1·8	6	50/ 72	6·48/6·44	0·98/1·05	LS	Test lateral capacity post L1W

*h is the loading height above ground level.
†Test 25 was part of the first-time axial test programme and was not subjected to lateral loading.

(*a*) fourteen large-diameter (LD) 508 mm dia. open-ended tubular high-yield-strain (grade API 5L X80) steel piles with length-to-diameter (L/D) ratios of 6 and 20, and 20·6 mm wall thicknesses (t) giving $D/t = 24{\cdot}7$
(*b*) two reaction (R) and test pile (TP) open-ended tubular piles with diameters of 1220 mm and 1800 mm (grades S460 and S355, respectively) and L/D ratios of 6 and 10, respectively. These piles had 24·6 mm and 25·0 mm thicknesses, giving $D/t \approx 50$.

The desired aim of delaying wall yielding before ground-level lateral displacements $v_G \geq D/10$ was largely achieved, although the longer 'LD' pile walls yielded shortly before reaching this displacement limit. All piles were fitted with strings of fibre Bragg grating (FBG) strain sensors in epoxy-filled grooves along the pile length, in a similar way to the PISA piles (Byrne *et al.*, 2020a; McAdam *et al.*, 2020), which all survived driving to be fully operational during testing. Sensors were positioned at 12 shaft levels for the LD piles and up to 29 along the longer 'R' and 'TP' piles, as defined in Jardine *et al.* (2023). Pile LD14, employed in the biaxial lateral cyclic (BLC) test, had four strings equally spaced circumferentially and a temperature sensor. Steady embedded pile temperature sensor measurements during lateral testing meant that FBG strain measurements did not require temperature correction during testing, as with the PISA pile tests. Buckley *et al.* (2020) and Jardine *et al.* (2023) describe the driving operations and the resistances inferred from dynamic and FBG sensors during driving and monotonic axial testing. As noted by Ciavaglia *et al.* (2017) and Buckley *et al.* (2018), driving causes extensive chalk damage around the open steel piles. Annuli of very soft 'putty' chalk formed around the shafts of piles (with diameters between 139 and 1220 mm) driven at SNW, with radial thickness similar to the piles' walls. A second annular region of damaged chalk was identified beyond the putty zone in which the chalk showed substantially increased fracturing, leading to notably lower stiffness and operational shear strength (Pedone *et al.*, 2023). The fracture spacings reduced most significantly in a region that extended out radially to approximately $7t_w$ from the shafts, with fracture spacings returning to their natural

intensity at radial distances of $12 \pm 2t$ from the pile shafts. While the putty chalk gained strength as the piles aged, the fracture damage was permanent. Pedone *et al.* (2023) showed that the radial ground displacements that develop in response to lateral pile loading concentrate principally within these two zones of 'driving-damaged' chalk. Previtali *et al.* (2023) showed how large-displacement particle FEM (PFEM) analyses incorporating a 'sensitive' chalk constitutive model calibrated to laboratory tests can capture some of the features observed during the installation of the open ALPACA piles.

TESTING PROGRAMME AND PROCEDURES

Types

Monotonic lateral static (LS), one-way cyclic (L1W) and BLC lateral tests were carried out. LS and L1W experiments involved loading paired piles against each other through bars tensioned by proportional–integral (PI) controlled hydraulic actuators and with load cells connected to each pile, as shown by the example LD pile illustration in Fig. 2(a). Loading arrangements distributed the load over the rear section of each pile. The lateral biaxial cyclic test involved applying one-way cyclic loading along one axis, while maintaining steady lateral loading on a perpendicular axis, with each axis controlled by a separate PI control loop: see Fig. 2(b). The lateral biaxial cyclic test provides a benchmark dataset for calibration and validation of models that aim to capture foundation response under the biaxial loading conditions experienced commonly by OWTs; such loading has been demonstrated to be strongly influential in relation to the performance of piles driven in other geomaterials (Richards, 2019)

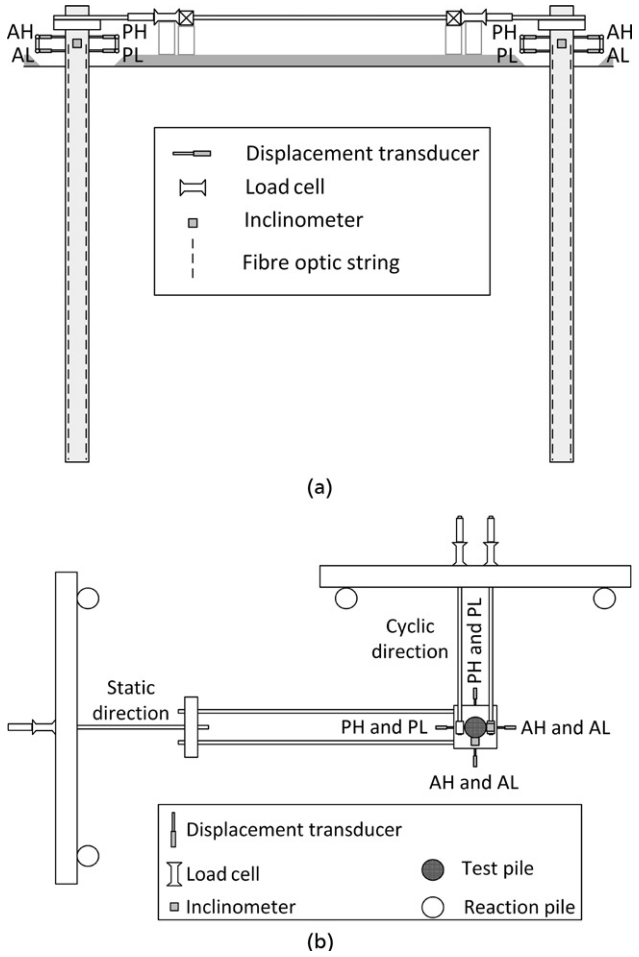

Fig. 2. Test schematics of fully instrumented (a) LD lateral static (LS) and cyclic (L1W) test and (b) Ø508 mm biaxial lateral cyclic (BLC) test plan view. Displacement transducer labels correspond to: AH – active high; AL – active low; PH – passive high; PL – passive low

Most lateral tests followed an earlier axial test (see Jardine *et al.* (2023) and Buckley *et al.* (2023)), in which plastic straining and shear failure were concentrated in thin interface annuli of 'putty' chalk. Numerical analyses by Pedone *et al.* (2020) indicated that these prior axial loading stages had little or no impact on the piles' subsequent lateral loading behaviour. The impact of axial loading is localised within the pile–chalk interface and the adjacent destructured chalk, as noted also in later analyses by Wen (2023) and Wen *et al.* (2023, 2024).

Programme

Table 1 lists the tests conducted after extended periods of ageing in situ (see Jardine *et al.* (2023)), numbered in chronological sequence, while Table 2 gives the minimum and maximum loads, $H_{\min}$ and $H_{\max}$, normalised cyclic loads, $H_{\text{mean}}/H_{D/10}$ and $H_{\text{cyc}}/H_{D/10}$ (where $H_{D/10}$ is taken as the load achieved at $v_G = D/10$), the cyclic loading characteristics, ζ_b and ζ_c, defined by LeBlanc *et al.* (2010a) as

$$\zeta_b = \frac{H_{\max}}{H_{D/10}} = \frac{H_{\text{mean}} + H_{\text{cyc}}}{H_{D/10}} \tag{1a}$$

$$\zeta_c = \frac{H_{\min}}{H_{\max}} = \frac{H_{\text{mean}} - H_{\text{cyc}}}{H_{\text{mean}} + H_{\text{cyc}}} \tag{1b}$$

as well as the number of cycles applied, N. All cyclic tests involved an initial 1000–2000 load cycles ('set 1'). In most cases, where piles had accumulated little displacement over set 1, additional 'set 2' cycles of higher amplitude were applied. The bilateral (BLC) testing progressed similarly, with the perpendicular static load being adjusted for each load set (Table 3). Axial static tension tests (ASTs) were carried out on three piles after lateral cycling; the final stage of all lateral cyclic tests involved monotonic lateral loading to failure.

Above-ground instrumentation

Two strain-gauged load cells and four potentiometer displacement transducers (DTs) were employed (per pile) in the LS and L1W tests, doubling these up for the BLC tests. When feasible, DTs were mounted against both the active (A) and passive (P) faces at both low (L) and high (H) positions to measure displacements relative to a reference beam. When space constraints made active measurement difficult, extra passive-face DTs were mounted at duplicated L and H locations. Rotation was measured by Geokon 6155 MEMS inclinometers, mounted on the pile wall perpendicular to the loading direction. Additional DTs were placed on the loading ram to aid test control. The load cell and DT ranges were optimised for each test and updated as required. Tarpaulin tented covers reduced the influence of rain, wind and sunlight on the sensors and reference beams; air temperatures were recorded close to the instruments. Positional surveys were made of all the above-ground instruments and loading pins with a total station throughout testing.

Table 2. Lateral one-way cyclic tests on LD piles

Test	Pile	Set	$H_{D/10}$: kN	H_{min}: kN	H_{max}: kN	$H_{mean}/H_{D/10}$	$H_{cyc}/H_{D/10}$	ζ_b	ζ_c	N	$v_{G,max}$: mm	$v_{G,final}$: mm
16	LD08	1	1465*	8	451	0·16	0·15	0·31	0·02	1500	8·42	−0·37
	LD10	1	1465*	8	451	0·16	0·15	0·31	0·02	1500	11·16	3·11
	LD08	2	1465*	30	1010	0·35	0·33	0·69	0·03	1000	34·54	0·38
	LD10	2	1465*	30	1010	0·35	0·33	0·69	0·03	1000	42·02	11·51
19	LD04	1	1465*	8	758	0·26	0·26	0·52	0·01	2000	18·81	3·52
	LD03	1	1465*	8	758	0·26	0·26	0·52	0·01	2000	25·62	8·11
22	LD01	1	1465*	457	767	0·42	0·11	0·52	0·60	1000	14·48	2·21
	LD09	1	1465*	457	767	0·42	0·11	0·52	0·60	1000	19·15	2·34
	LD01	2	1465*	262	1027	0·44	0·26	0·70	0·26	1000	32·60	6·58
	LD09	2	1465*	262	1027	0·44	0·26	0·70	0·26	1000	44·45	11·06
27	LD05	1	1465*	565	1025	0·54	0·16	0·70	0·55	1000	30·30	2·68
	LD02	1	1465*	565	1025	0·54	0·16	0·70	0·55	1000	36·50	3·46
	LD05	2	1465*	8	1224	0·43	0·42	0·84	0·01	913†	56·90	14·19
	LD02	2	1465*	8	1224	0·43	0·42	0·84	0·01	913†	59·12	11·24
+4	R1	1	7435	75	1867	0·13	0·12	0·25	0·04	1005	15·72	6·03
	R1	2‡	7435	75	4107	0·28	0·27	0·55	0·02	261	52·13	21·23
	R1	3	7435	75	1867	0·13	0·12	0·25	0·04	256	45·77	23·00

*Load at $v_G = D/10$ based on extrapolation of monotonic load behaviour in test 15 (see Fig. 4(a)).
†Load cell failure at approximately 885 cycles and test terminated at 913 cycles – no sign of pile failure.
‡Loading rate reduced from 0·1 Hz to ≈1/120 Hz at latter stages of load set.

Table 3. Lateral biaxial cyclic test results on LD piles

Test	Pile	$\overline{H}_{D/10}$*: kN	H_{min}: kN	H_{max}: kN	H_{stat}: kN	$H_{mean}/\overline{H}_{yield}$	$H_{cyc}/\overline{H}_{D/10}$	$H_{stat}/\overline{H}_{D/10}$	ζ_b	ζ_c	N	$v_{G,max}$: mm cyc/stat	$n = 500$ $v_{G\ acc,stat}$: mm
30	LD14	1465	14	459	230	0·16	0·15	0·16	0·31	0·03	1000	4·1/4·1	7·44
	LD14	1465	23	1071	536	0·37	0·36	0·37	0·73	0·02	1000	40·2/54·0	60·2

*Equivalent to average $H_{D/10}$ in test 15.

Procedures

The LS tests were controlled by a PI feedback loop from a passive low (PL) side DT. They ran at a ground-level displacement rate of approximately $D/300\,\text{min}^{-1}$ until the target v_G steps shown in Fig. 3(a) were achieved. Each step included a maintained load stage over which displacements were monitored. Loading resumed once the displacement creep rate fell below 0·001% of D per minute, or the creep stage duration exceeded 30 min. The monotonic tests, whose procedures were optimised as testing progressed, generally allowed the $v_G = D/10$ targets to be met within several hours. These durations may be compared with broad estimates of the dissipation times required for any pore pressures generated around the test piles by lateral loading. Applying a broadly analogous plane-strip loading solution from Schiffman *et al.* (1967) and the mean $c_{vh} = 7 \times 10^4$ m^2/year radial consolidation coefficient from piezocone dissipation tests (Vinck *et al.*, 2022) suggests t_{95} times the order of 5 and 30 min for the 508 mm and 1200 mm dia. piles, respectively. However, shorter times are likely to apply in the field, given the additional fracturing caused to the chalk by pile driving, leading Pedone *et al.* (2023) to consider the slow monotonic tests as fully drained, as proposed earlier for larger foundations by Lord *et al.* (2002).

The $L/D = 6$ by 508 mm dia. piles (LD12 and LD13) reached geotechnical failure at $v_G = D/10$ before their steel walls yielded. However, the most heavily loaded sections of the longer LD, R and T piles yielded at axial strains of 2613 $\mu\varepsilon$ and 2050 $\mu\varepsilon$ for their X80 and S460 steels, respectively (with yield bending moments of 2027 kNm and 5700 kNm) before reaching $v_G = D/10$. The piles were unloaded at strains slightly below these limits (7%) before imposing further loading loops. The LS test loading procedures generally comprised:

(*a*) loop 1 – initial low-level monotonic loading to between approximately 1·2 MN for the LD piles and 5·7 MN for the larger piles
(*b*) loop 2 – continuous reloading to the maximum loop 1 displacement, followed by unloading
(*c*) loop 3 – continuous loading to the maximum ram stroke, followed by unloading
(*d*) loop 4 – continuous reloading to the maximum loop 3 displacement, followed by unloading.

Different procedures were adopted for tests 15 and 18 (only loop 1) and loop 4 was not applied in test 28.

The L1W and BLC tests applied sinusoidal (in time) loading cycles with constant load amplitudes (H_{cyc}) and mean (H_{mean}) values. A cyclic frequency ≈ 0·1 Hz (period 10 s) was maintained in most tests (see Table 2). The cyclic tests typically extended for 3 to 6 h, and sometimes longer. Excess pore pressures are likely to have largely dissipated as the tests progressed. Cyclic failure was pre-defined as the peak v_G displacements growing by more than 0·5 mm over a single cycle, or permanent v_G displacements exceeding $D/10$. However, no such cyclic failure occurred in any test.

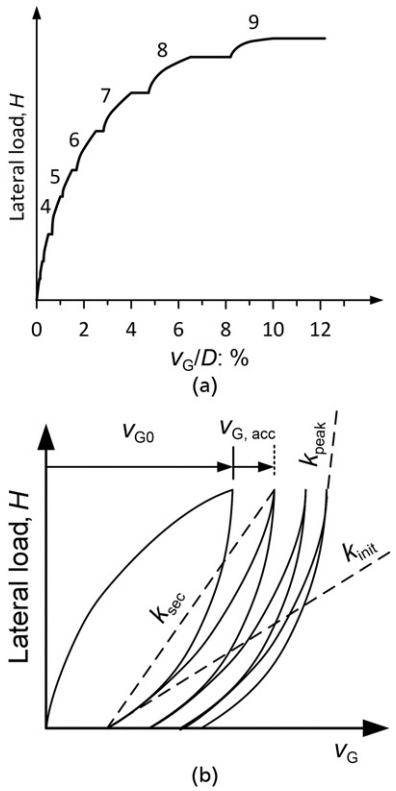

Fig. 3. Schematic illustrations of (a) monotonic load–displacement curve and (b) one-way cyclic displacement and stiffness parameters

Data acquisition

All load, displacement and inclination measurements were logged with 16-bit resolution through proprietary Tiab and Campbell data acquisition systems. A Campbell system also acquired thermocouple data with 13-bit resolution. The FBG strains were interrogated with a Micron Optics SM130. Time-source pulses and a network time protocol hosted in the Campbell logger enabled Tiab and Micron Optics system synchronised data post-processing.

Data processing

The measured displacements and rotations were converted to ground surface v_G, and rotation, θ_G, measures by applying a calibrated Timoshenko beam model of the pile above ground, after Burd *et al.* (2020a). It was necessary to smooth the inclinometer signals using a zero-phase digital filter, which applies a Gaussian window (with 1·5 s width) of 15 samples in both the forward and reverse filtering directions. Any gauges that exceeded their working limits were excluded or replaced. The pile bending moments were calculated from the FBG strains, $\Delta\varepsilon$, from equation (1):

$$M = \frac{\Delta\varepsilon EI}{D} \tag{1}$$

where E = 210 GPa for the steel; I is the pile's second moment of area; and D is the pile outer diameter.

INTERPRETATION AND RESULTS

Backbone load–displacement curves

To provide a clear comparison between tests, monotonic loading 'backbone' curves were established for each test. As described by Byrne *et al.* (2020a) piecewise cubic splines were fitted to the highest displacement rate sections of the load–displacement traces. The curves characterise the response over the first loading cycle and any subsequent loading stages that exceed the maximum previous load. Where required, they also allow systematic extrapolation of the loads expected at $v_G = D/10$.

As noted earlier, pile displacements grow over time during maintained load 'creep' stages. Such time-dependent measurements can be interpreted to infer families of load–displacement curves that display isotach, rate-dependent, behaviour; see Pellew (2002) or Pellew & Jardine (2008). The 10 s cyclic test periods imposed significantly higher loading rates than the slow monotonic tests, and the chalk's rate dependency led to most cyclic backbone curves locating above the monotonic loading relationships.

Virgin monotonic loading load–displacement curves

Virgin lateral monotonic ground-level load displacement test data are shown in Figs 4(a) and 4(b) for pairs of long (L/D = 20) and short (L/D = 6) LD piles, plus for the short (L/D = 6) TP2 pile in Fig. 4(c) and in Table 4. Steel yield occurred in the long LD tests before v_G reached $D/10$. Single piecewise cubic splines, fitted as shown in Fig. 4(a), were used to extrapolate the backbone curves to ultimate load estimates of $H_{D/10}$ of 1392 kN and 1534 kN for LD06 and LD11, respectively, typically 10 to 20% above the maximum applied. The small final permanent displacements ($\approx D/100$) reached after the LD06 and LD11 tests' markedly non-linear unloading stages indicates that these piles behaved flexibly over their deeper anchoring sections, rather than rotating as rigid bodies. However, local failure in front of the piles was demonstrated by the open ground-level cracks observed after unloading, which correlated with the maximum ground-level displacements developed under loading.

Figure 4(b) shows the response of the 'short' LD12 and LD13 (L/D = 6) piles, which exhibited a more markedly plastic and non-reversible load–displacement response. Geotechnical failure, with $v_G = D/10$, was reached at 1011 kN and 983 kN for LD12 and LD13, respectively, well before steel yielding. Near-rigid rotation was confirmed by analysis of the strain gauge data, as outlined below. Relatively large displacements were developed when even small reloading increments were applied when $v_G > D/10$, reflecting the brittle failure in the chalk around the shaft, which penetrated to progressively greater proportions of the pile length. Reloading to levels exceeding those applied previously allowed the load–displacement response to re-join and extend the virgin-loading backbone curve. The permanent ground-level displacements, $v_{G,final}$, of 90·7 mm and 104·6 mm, respectively ($\approx D/5$), developed after final unloading were over 20 times those developed by the long LD piles.

Figure 4(c) shows the response of TP2 (L/D = 6), which exhibited a similar shape, but lower level of residual displacement compared to the smaller diameter L/D = 6 LD piles. Steel yield was anticipated to occur at approximately 5·7 MN for TP2, about 25% below the load measured at $v_G = D/10$. The later stages of the post-cyclic monotonic test on R1, which are also shown, appear broadly compatible with the TP1 backbone curve.

Application of beam theory to deduce soil reactions, pile moments and displacements

Profiles of distributed lateral load, bending moment and displacement at peak load were interpreted from the embedded Timoshenko beam differential equation, following Byrne *et al.* (2020a). The piles were split into five segments

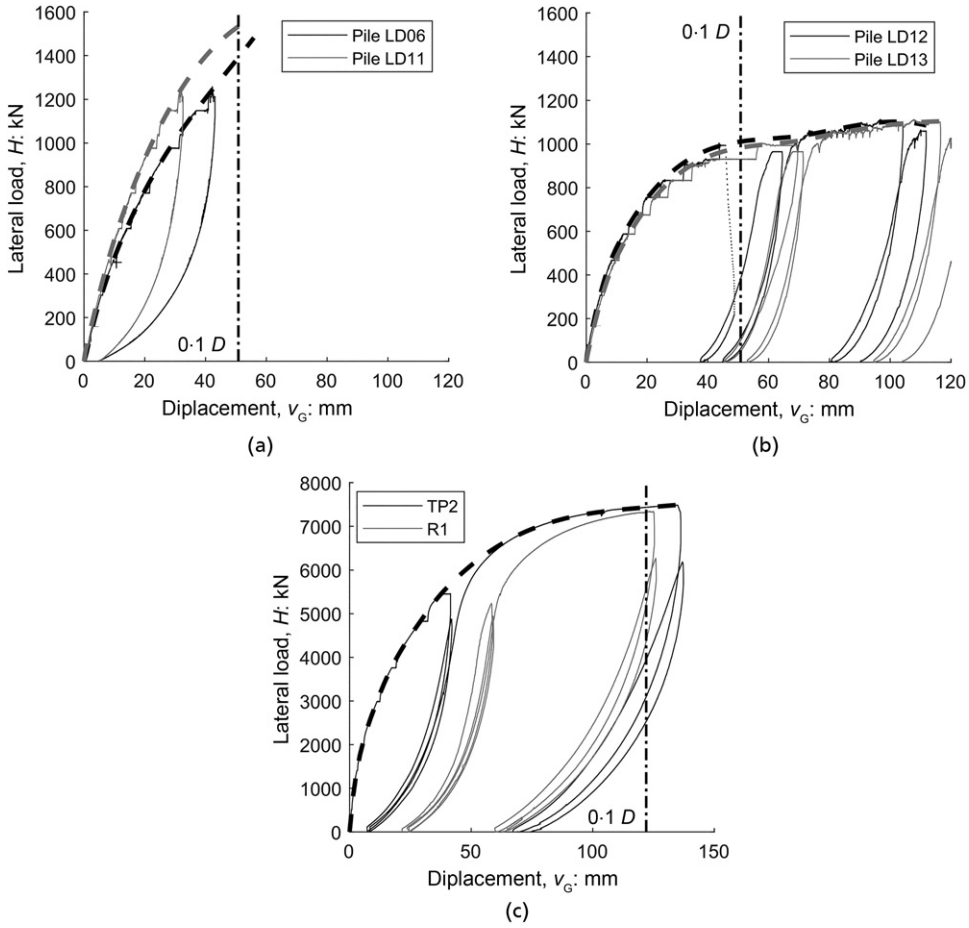

Fig. 4. Load–displacement response for first-time lateral monotonic tests: (a) test 15 (L/D = 20); (b) test 26 (L/D = 6); and (c) test +3 (L/D = 6) and test +5 post-cyclic monotonic, with fitted backbone spline curves shown with dashed lines. A temporary period of logging error for LD12 is indicated by dotted lines in (b)

Table 4. Summary of monotonic lateral test results

Test	L/D	Piles	$H_{D/10}$: kN	k_{init}: kN/m	$v_{G,final}$: mm
15	20	LD06	1392	44 753	4·7
	20	LD11	1534	86 168	4·8
18*	20	LD08	—	12 517	4·2
	20	LD10	—	15 792	14·1
21*	20	LD03	—	38 991	44·8
	20	LD04	—	17 444	37·5
24*	20	LD01	1677†	12 029	52·3
	20	LD09	1571†	51 172	59.7
26	6	LD12	—	114 950	90.7
	6	LD13	—	78 166	104·6
28*	20	LD02	—	46 497	63·2
	20	LD05	—	27 049	40.6
32*	20	LD14	—	—	39.6
+3	6	TP2	7435	576 973	73·0
+5*	6	R1	7327†	—	62·7

*Post-cyclic monotonic test.
†$H_{D/10}$ response interpolated from post-cyclic monotonic backbone.

below ground level. The bending moments from FBG strains, measured loads, displacements and rotations provided the necessary objective parameters. Assuming the soil reactions as continuous along the pile and varying linearly within pile segments led to a set of linear equations from which load and deformation distributions were obtained.

Considering the first loading set (in test 16) on a typical L/D = 20 pile, LD10, shown later in Fig. 9(a), Fig. 5 shows that peak bending moments (and their depths of occurrence) grew as the chalk to pile gap extended down the shaft with cyclic loading. While the L/D = 20 piles responded flexibly at depth, their anchor points gradually migrated down the shaft as top-down local stress redistribution progressed with increasing N. In contrast, the cyclic test on the larger diameter R1 (L/D = 6) pile demonstrated behaviour closer to the rigid monotonic loading response shown by the smaller diameter LD (L/D = 6) piles. Significant residual displacements were observed over a larger proportion of the embedded pile length, indicating far greater mobilisation of the chalk strength.

The beam analysis also allowed local soil $p(z)$ profiles and p/D–v reaction curves to be deduced from the monotonic and cyclic loading tests. No characteristic length was applied to normalise the local lateral deflections, as this choice led to the most successful subsequent back-calculation of the pile responses observed at three scales. Noting that the LD and R/TP piles had quite different diameters D (0·508 m and 1·22 m) and less divergent wall thicknesses t (20·6 mm and 24·6 mm), the narrow spread of field p/D–v curves shown in Figs 6(b)–6(d) suggests that the normalising characteristic length for the soil reaction displacements cannot be, as in clays, simply the pile diameter D. The characteristic length may be affected by the fracture spacings in the chalk that result from the damaging process of pile driving, with distributions that depend on the pile

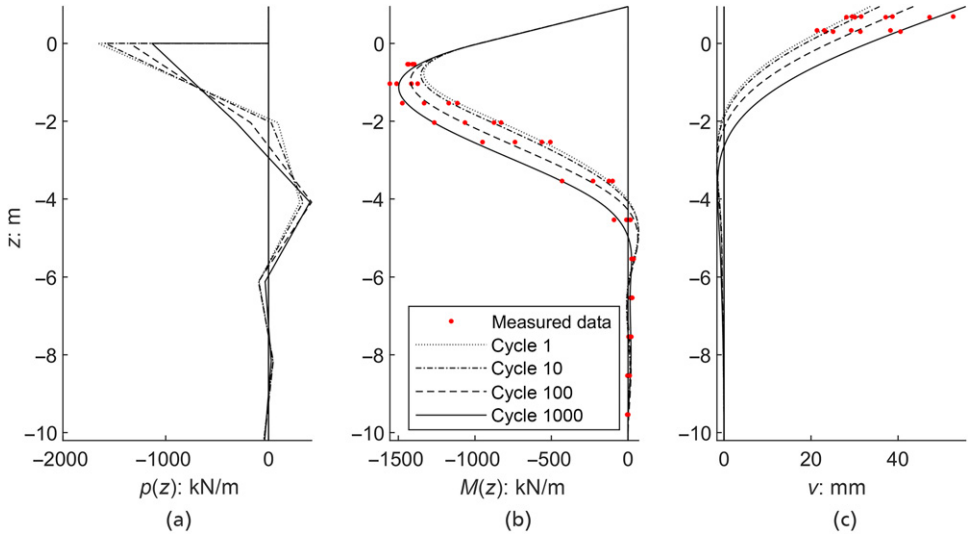

Fig. 5. Profiles of (a) distributed lateral load, (b) bending moment, including bending moment data inferred directly from the fibre optic strain gauges, and (c) lateral displacement, including displacement transducer measurement during the uni-directional lateral cyclic test on LD10 (test 16)

wall thickness, t. Further testing or advanced numerical modelling is required to determine robustly the most appropriate normalising combination of D and t.

Consideration of the deformation measurements made close to ground level, and the assumption of pile toe fixity, allowed consistent depth-wise calculation of the monotonic p/D–v reaction curves for L/D = 20 piles shown for LD11 in Fig. 6(b). Also shown are the equivalent curves calculated for the L/D = 6 piles, LD13 in Fig. 6(c) and TP2 in Fig. 6(d). Greater scatter was observed for the latter piles,

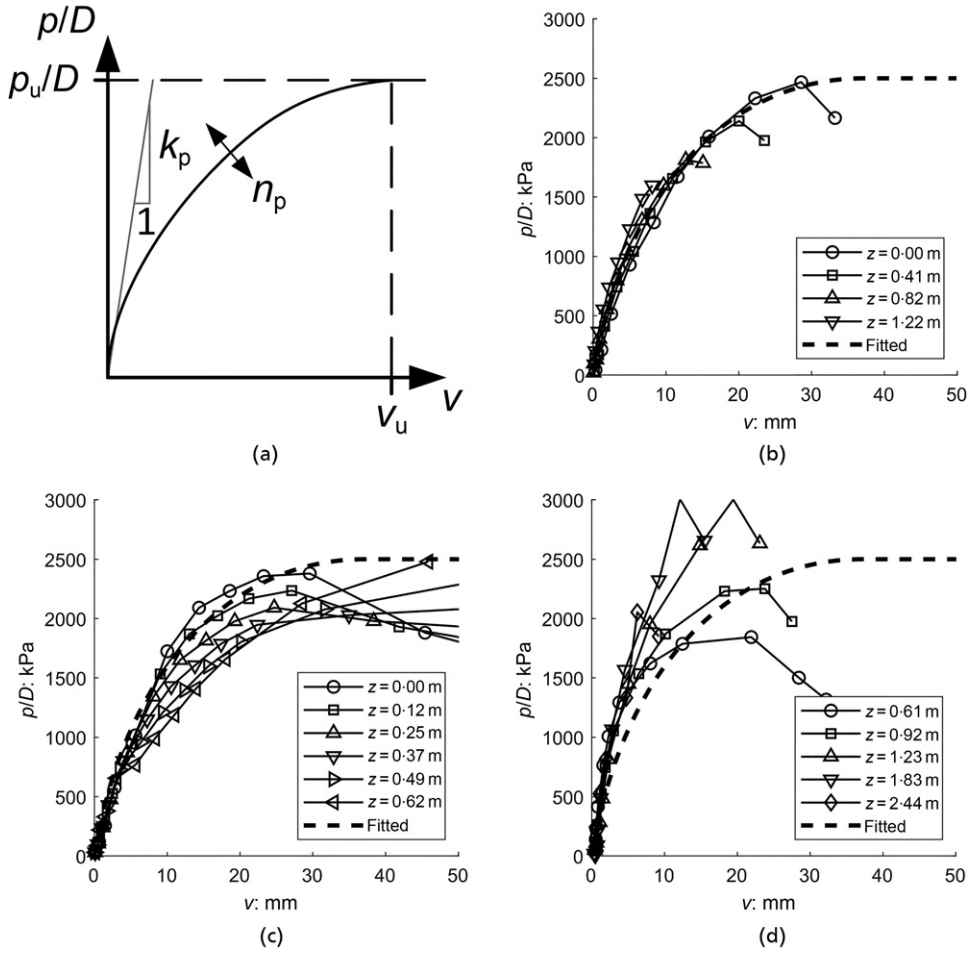

Fig. 6. Soil reaction curves for normalised distributed lateral load: (a) non-dimensional form of PISA p–v curve and extracted from (b) long LD pile LD11, (c) short LD pile LD13 and (d) short pile TP2 data

whose displacement–depth profile is affected by uncertainty over pile toe deformations, a difficulty that can be overcome by deploying additional in-place inclinometers (Byrne *et al.*, 2020b). Also, the soil reactions could not be determined reliably at depths greater than 1·5 to 2*D*, due to the proximity of the piles' points of rotation. Despite these challenges, the paired tests on LD06 and LD13 led to similar p/D–v curves.

Simplified reaction curve-fitting analyses have also been undertaken with equation (2), a generalised form of the PISA p–v curve (Byrne *et al.*, 2020b), as shown in Fig. 6(a), where $\overline{p} = p/D$. The defining parameters are the limiting distributed lateral load, p_u, the initial stiffness k_p, the ultimate displacement v_u and a curvature parameter, n_p.

$$-n\left(\frac{\overline{p}}{\overline{p}_u} - \frac{v}{v_u}\right)^2 + (1-n)\left(\frac{\overline{p}}{\overline{p}_u} - \frac{vk_p}{\overline{p}_u}\right)\left(\frac{\overline{p}}{\overline{p}_u} - 1\right) = 0 \qquad (2)$$

A single, depth-independent reaction curve is fitted to the interpreted reaction curve from the L/D = 20 pile LD11 in Fig. 6(b), assuming p_u/D = 2·5 MPa. Least-squares fitting led to best-fitting k_p = 386 MPa/m, v_u = 0·0371 m and curvature, n_p = 0·705 values. This distributed lateral soil reaction curve incorporates the influence of the additional soil reaction components that could not be disaggregated from the Timoshenko beam analysis. Application in 1D FE beam modelling enabled back-calculation of the bending moments and ground level load–displacement behaviour of the 'virgin' monotonic loading tests. As shown in Fig. 7, good fidelity within experimental variability is observed for the backbone curves of the LD L/D = 6 and 20 pile cases, the 1220 mm dia. TP2 pile and the 762 mm dia. short (L/D = 5) pile at the same site by Ciavaglia *et al.* (2017). It is observed that the single 'best-fit' soil reaction produces an excellent fit to the observed pile response, even if the local soil reaction fits are less good. This well-conditioned aspect of the model was identified in Burd *et al.* (2020b) and is attributed to the integration of the model over the pile depth, where different parts of the soil reaction curve are mobilised at different depths, which appears to average out local variations in model fit. Further development of the soil reaction curves for full-scale application, at both small and large displacement, would be likely to require a comprehensive set of numerical analyses, following the PISA numerical calibration methodology. It is likely to be beneficial for any such study to explore the sensitivity of the predicted behaviour to the adopted fitting parameters.

A key point to note from Fig. 6(b) is that the fitted ultimate lateral resistance p_u/D of 2·5 MPa does not vary with depth. This resistance may appear surprisingly low in relation to the laboratory UCS and triaxial shear strengths of intact SNW chalk. As noted earlier, Vinck *et al.* (2022) indicated a mean equivalent Tresca shear strength s_u = 1·32

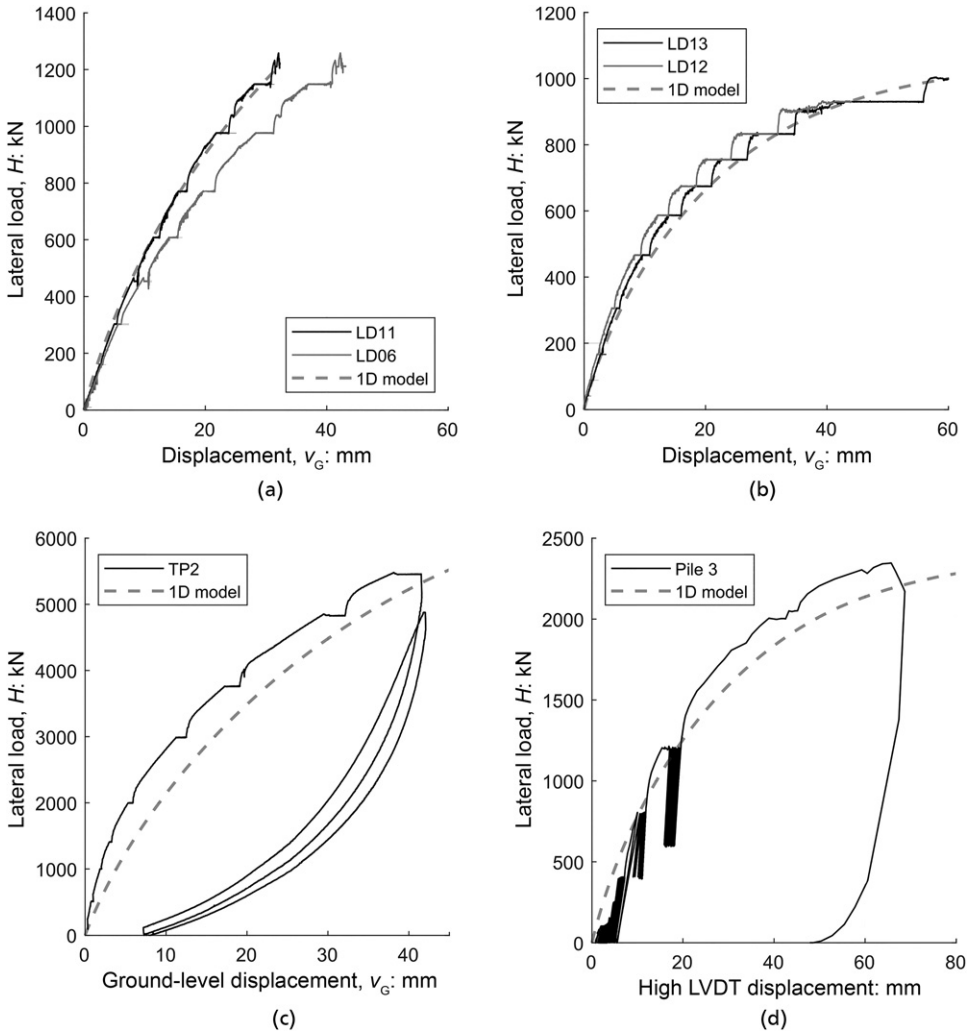

Fig. 7. Comparison of measured and 1D model calculations of monotonic tests: (a) test 15 (LD11 and LD06, Ø508 mm, L/D = 20); (b) test 26 (LD12 and LD13, Ø508 mm, L/D = 6); (c) test +3 (TP2, Ø1220 mm, L/D = 6); and (d) pile 3 (D = 0.762 m, L/D = 5) monotonic test from Ciavaglia *et al.* (2017). Note that LD12 data for v_G >44 mm in (b) are omitted due to a logging error

MPa over the relevant depth range, which implies a constant lateral bearing factor $N_c \approx 1{\cdot}9$, which falls far below those found analytically for undrained failure in ductile clays. Their N_c values typically rise with relative depth from ≈3 at ground level, where 'wedge failures' may apply, to ≈10 at depths where 'flow-around' mechanisms dominate (Murff & Hamilton, 1993). However, Pedone *et al.* (2023) showed that the L/D = 6 LD piles' load–displacement response and ultimate lateral capacity profile may be matched faithfully through effective stress-based 3D FE analyses that account for the damage caused by pile driving and the chalk's brittle, anisotropic and pressure-level-dependent mechanical behaviour.

It is also important to note that the piecewise polynomial fitting of lateral reactions and displacements, given the field test results described above, capture the influence of, but cannot delineate, the contributions of other soil reaction components, such as distributed moments, as recommended for PISA-style analyses (Byrne *et al.*, 2020a). However, these components can be obtained from representative numerical analyses in a similar manner to that described by Taborda *et al.* (2020) and Zdravković *et al.* (2020). The systematic approach set out by Pedone *et al.* (2023) provides the basis for deriving PISA-style 'four-component' reaction curves.

Cyclic loading

The ten phases of L1W cyclic tests completed are summarised in Table 2. For the LD piles the capacity $H_{D/10}$ is extrapolated as 1465 kN from monotonic lateral tests on LD06/LD11 (test 15), while $H_{D/10}$ is interpolated as 7435 kN for the larger diameter TP2 (test +3). Cycling was applied to all the LD L/D = 20 piles and to one larger diameter (L/D = 6) pile (R1). The cyclic loads were chosen to avoid steel yielding, keeping $H_{max}/\overline{H}_{D/10} < 0{\cdot}7$ and all single-axis cyclic tests reached their programmed (1000 or 2000 cycle) durations without failure.

Figure 8 summarises the LD L1W cyclic loading conditions in normalised interaction diagrams, which also specify normalised, $v_{G\,max}$, and accumulated, $v_{G\,acc}$, maximum displacements (defined in Fig. 3(b)) developed after 1000 cycles. The north-side piles tend to develop slightly higher movements than those to the south, reflecting local chalk variations. A general trend exists, however, for maximum displacement to grow with radius from the origin, while being more strongly influenced by cyclic load amplitude than the mean load.

Figure 9 presents typical load–displacement trends for varied single-amplitude cyclic load sets, as defined in Table 5. The first stage L1W cycling response of the L/D = 20 pile LD10 (test 16) presented in Fig. 9(a) shows permanent displacements, $v_{G,acc}$, accumulating relatively slowly over 1000 cycles. Loading to the second, higher, level of cycling featured a soft initial first cycle, as the gaps already present on the active and passive sides of the pile opened up to widths that were broadly compatible with the pile's ground-level displacements.

However, most cyclic load–displacement loops showed maxima that plot significantly above the monotonic backbone curves of identical adjacent piles. This feature is interpreted as reflecting (*a*) the chalk's compressibility and undrained shear strength being time dependent and rising by approximately 10% per log cycle of strain rate in laboratory tests (Vinck *et al.*, 2022) and (*b*) potential effects of partial drainage occurring around the pile shafts during testing. Fig. 9(b) shows how this hypothesis was checked by loading the pile LD02 approximately 80 times (or ≈1·9 log cycles) more slowly in test 27, taking 6·5 min to reach H_{min}, rather than the 2·5 s required when cycling at 0·1 Hz. This test's first loading cycle follows, as expected from the rate-dependent hypothesis, the monotonic backbone curve from the adjacent (LD11) pile far more closely before accumulating further displacements steadily as cycling continued. However, intrinsic chalk variability also led to cases where the cyclic loading peaks fell below the monotonic backbone curves, as shown for the L/D = 6 R1 pile in Fig. 9(c). The measured ground displacement at the start of the first cycle of each loading set, v_{G0}, is shown in Fig. 9(d). It is evident that the extrapolated test 19 monotonic behaviour, obtained from the mean of the first cycle response of the two piles, would provide a good estimate of v_{G0} for all tests.

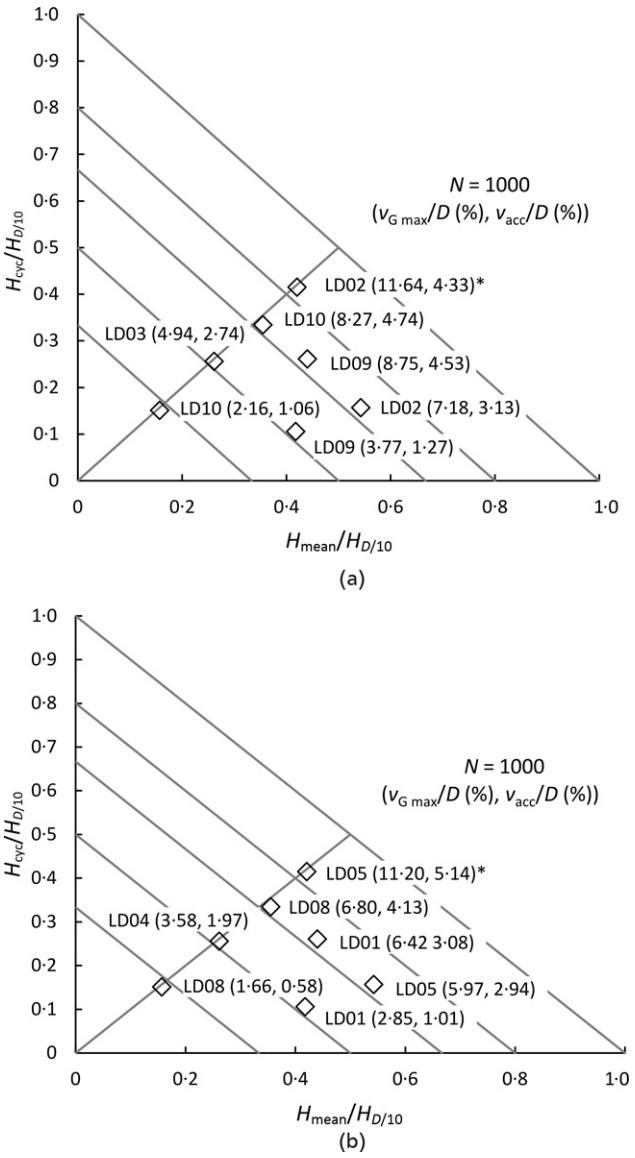

Fig. 8. Cyclic loading interaction diagrams with maximum ground-line displacement $v_{G\,max}$ (% of diameter) and accumulated ground-line displacement $v_{G\,acc}$ (% of diameter) at n = 1000 (a) north side (b) south side (*test equipment failure, data shown from last cycle at n = 913)

Figure 10(a) illustrates schematically how gapping under significant lateral load cycling creates additional free pile length that reduces the soil reactions and pile head stiffness. The gradual re-establishment of contact during reloading leads to pile head stiffness increasing during a loading cycle, leading to the stiffening cycle shapes shown in Fig. 9 with peak, k_{peak}, and overall secant, k_{sec}, cyclic stiffnesses (defined in Fig. 3) generally exceeding the initial, k_{init}, values.

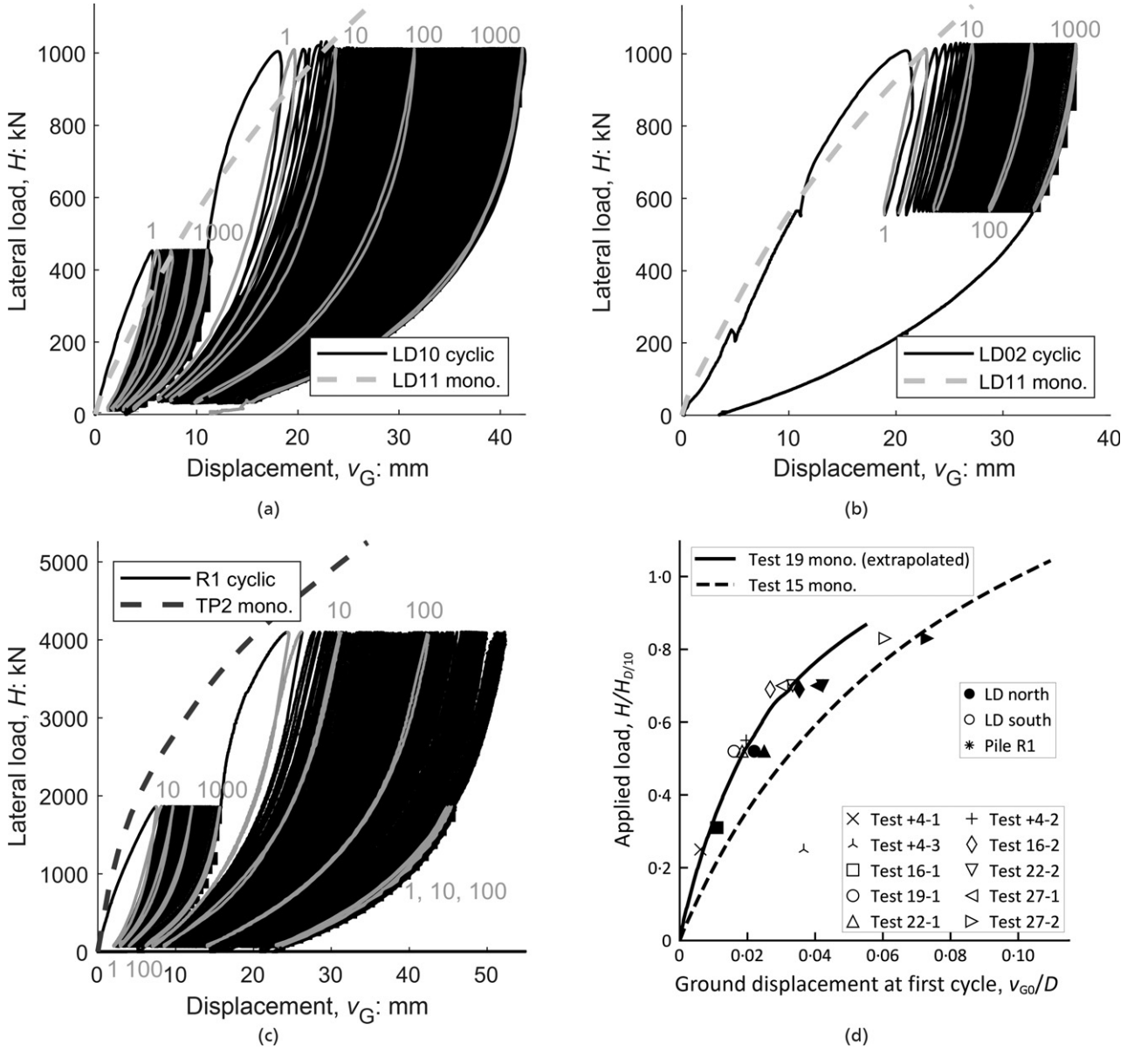

Fig. 9. (a) Load–displacement response on LD10 (test 16); (b) load–displacement response on LD02 (test 27-set 1); (c) load–displacement response on R1 (test 4). The monotonic backbone curve (mono.) from first-time loading (see Fig. 4) is shown with dashed lines. Cycles 1, 10, 100 and 1000 are highlighted and labelled. (d) Normalised ground displacement at the start of each set of cycles

Table 5 lists the salient displacements and stiffnesses at virgin loading, first cycle and at $n = 500$ cycles. The evolution of stiffness in test 16 (on pile LD10), a typical two-stage cyclic experiment, is illustrated in Fig. 10(b). The k_{init} stiffness seen on virgin loading ($n = 0$) in set 1 was 114·8 MN/m, which fell to 54 MN/m after the first cycle ($n = 1$) due to gap formation, before settling at a steady ≈ 25 MN/m for the next 1000 cycles, then reducing further to ≈ 12 MN/m in set 2. The k_{sec} traces show a more gradual and moderate reduction with cycle number. The observed stiffness trends have important implications for the piles' in-service response to small load cycles, which may affect the dynamic behaviour of the structure they support.

The patterns of maximum cycle displacement, $v_{G,max}$ (normalised by $D/10$), are illustrated for the pairs of piles loaded in the LD cyclic test Fig. 11. In all cases the incremental accumulated displacements appeared to reduce with increasing numbers of cycles, and there were no instances of catastrophic or 'run-away' behaviour. LeBlanc *et al.* (2010a) proposed a power-law relationship to model accumulated displacement (or rotation) observed for constant-amplitude cycling in model pile tests:

$$\frac{v_{G,acc}}{v_{G,s}} = \frac{v_G(N) - v_{G0}}{v_{G,s}} = T_b(\zeta_b)T_c(\zeta_c)N^{\alpha} \quad (3)$$

where $v_{G,s}$ is the ground level displacement that is predicted to occur in a static (monotonic) test to H_{max}; v_{G0} is the displacement at the start of cycling; α is a fitting exponent, originally chosen as $\alpha = 0.31$; and $T_b(\zeta_b)$ and $T_c(\zeta_c)$ are dimensionless functions depending on the cyclic load characteristic parameters, ζ_b and ζ_c, respectively. For rate-independent behaviour it would be expected that $v_{G,s}$ and v_{G0} are equal. The former captures the influence of the peak load of the cycling, while the latter captures the influence of the asymmetry (or lack thereof) of the cycling.

Table 5. Lateral one-way cyclic tests on LD piles

Test	Pile	Set	$v_{G,max}$: mm		$v_{G,acc}$: mm		k_{init}: MN/m		k_{sec}: MN/m		k_{peak}: MN/m
			$n = 0$	$n = 500$	$n = 1$	$n = 500$	$n = 0$	$n = 500$	$n = 0$	$n = 500$	$n = 500$
16	LD08	1	5·51	8·42	0·39	2·91	65·83	17·60	82·00	59·30	218·38
	LD10	1	5·60	10·64	0·48	5·04	114·75	24·89	79·34	61·20	174·57
	LD08	2	13·58	32·17	1·45	18·59	21·12‡	10·62	78·43‡	36·15	205·45
	LD10	2	17·95	39·22	1·63	21·28	22·70‡	12·42	69·60‡	38·15	143·12
19	LD04	1	8·14	17·34	1·03	9·20	118·67	17·03	91·26	54·93	198·74
	LD03	1	11·17	24·26	1·42	13·09	88·42	16·82	66·80	42·90	159·62
22	LD01	1	9·37	13·72	0·07	4·34	*	174·86	*	227·58	496·65
	LD09	1	12·68	18·42	0·10	5·74	*	105·30	*	158·55	322·67
	LD01	2	16·94	30·12	0·10	13·18	*	25·95	*	77·77	292·70
	LD09	2	21·43	40·51	0·14	19·08	*	25·23	*	63·31	197·29
27	LD05	1	15·36	29·32	1·82	13·95	97·28	64·34	52·08	144·34	249·60
	LD02	1	20·60	35·63	1·92	15·03	89·15	64·80	46·38	116·00	283·53
	LD05	2	30·79	52·37	0·25	21·57	12·99‡	9·27	42·70‡	32·94	209·05
	LD02	2	37·12	56·57	0·33	19·45	9·41‡	8·18	34·19‡	28·67	155·45
+4	R1	1	7·45	14·46	0·67	7·01	368·81	80·89	239·48	193·61	538·97
	R1	2	23·94	42·31†	1·98	18·37†	41·03‡	47·95†	208·96‡	140·50†	479·14†
	R1	3	44·68	45·39†	0·52	0·71†	19·65‡	38·40†	75·05‡	82·00†	163·24†

*Stiffness during cycling not available due to loading beginning from H_{max}.
†Data for $n = 100$ cycles, as fewer than $n = 500$ cycles completed.
‡Loading following a lower prior cycling package.

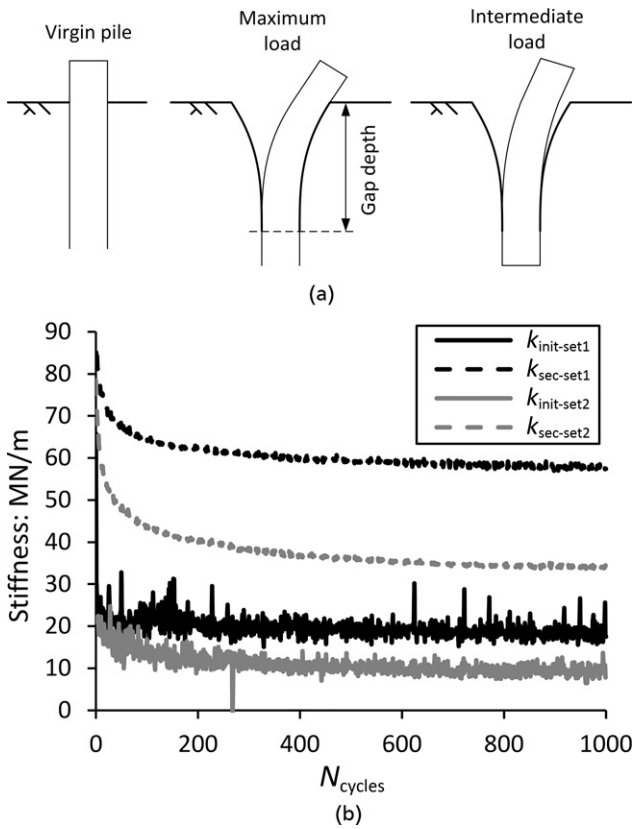

Figure 10. Onset of gapping during lateral loading: (a) illustration of development and influence of gap and (b) evolution of k_{init} and k_{sec} stiffnesses with cycle number for pile LD10 during test 16 where $n = 0$ values of $k_{init-set1} = 114·8$ MN/m, $k_{sec-set1} = 79·3$ MN/m, $k_{init-set2} = 22·7$ MN/m and $k_{sec-set2} = 69·6$MN/m

The model calibration process is shown in Fig. 12. The $v_{G,acc}$ observed at the peak of each cycle is normalised by $v_{G,s}$, hich was obtained from the extrapolated test 19 monotonic backbone curve shown in Fig. 9(d), as this seems to give a reasonable prediction for all tests. The results are plotted in Fig. 12(a) for $\zeta_c \leq 0·06$ (one-way tests) and Fig. 12 (b) $\zeta_c > 0·06$ (partial one-way tests), which are used to calibrate the $T_b(\zeta_b)$ and $T_c(\zeta_c)$ functions, respectively. A value of $\alpha = 0·28$ was found to best match the test data, which is in close agreement with the original study by LeBlanc *et al.* (2010a), as well as the interpretation by Beuckelaers (2017) of the PISA cyclic tests at two different sites. This perhaps indicates that pile ratcheting behaviour is reasonably consistent for different sites and different pile geometries. An intercept value, equivalent to the product $T_b(\zeta_b)T_c(\zeta_c)$, was fitted to each test. By convention, for one-way tests $T_c(0) = 1$, which allows the $T_b(\zeta_b)$ values to be extracted from Fig. 12(a) directly and plotted in Fig. 12(c). The following function was then fitted to these data:

$$T_b(\zeta_b) = 0·27\sqrt{\zeta_b} \tag{4}$$

This fits the majority of the data well, although the fit is less good for tests +4-3 and 27-2, which were both preceded by cycles with a particularly high peak load (i.e. these tests were conducted from an initial overloaded state). LeBlanc *et al.* (2010b) set out a process that can be used to account for different amplitudes of cycling, by superimposing the effects of each set of cycles.

$T_c(\zeta_c)$ values were obtained by comparing the intercept of each test with a corresponding one-way test with the same ζ_b value. These are shown in Fig. 12(d), where the following function was chosen:

$$T_c(\zeta_c) = 1 - \zeta_c \tag{5}$$

This agrees well with tests 22-1 and 22-2, but test 27-1 is an outlier. This is probably due to a slower rate of initial loading for this test, reducing $v_{G,s}$, which is perhaps not captured as well in this simple model. When considering the mean values from paired pile tests and when excluding those pile tests that are outliers (test 27-1, test 27-2 and test +4-3) the model predicts T_b and T_c with R^2 values of 0·90 and 0·96, respectively.

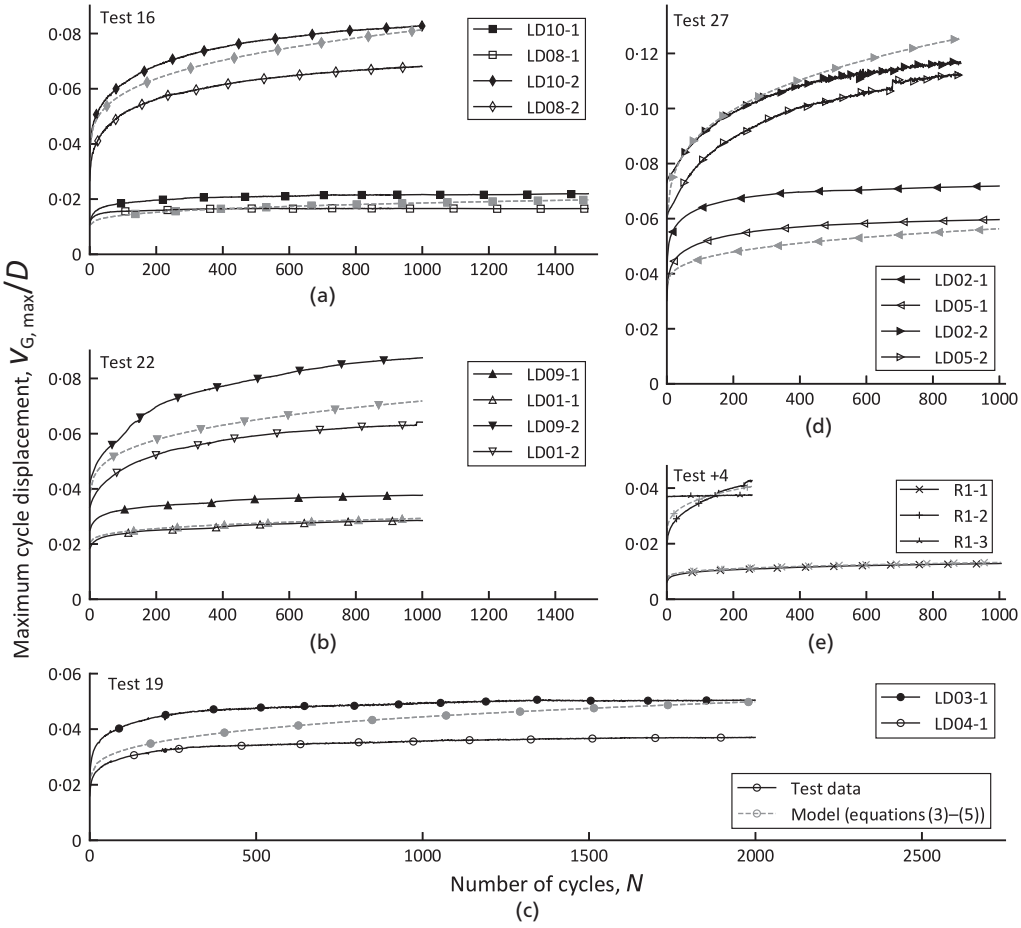

Fig. 11. Measured permanent accumulated cyclic displacement normalised by D and results from the modelling using equations (3)–(5) for: (a) test 16; (b) test 22; (c) test 19; (d) test 27; and (e) test +4

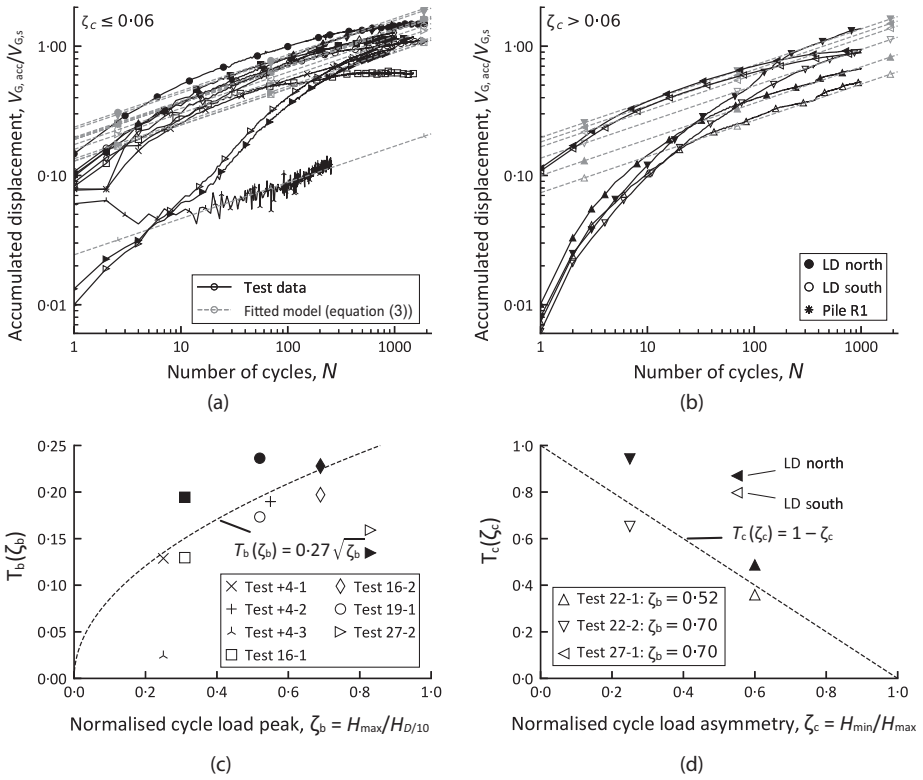

Fig. 12. (a), (b) Permanent accumulated cyclic displacement normalised by predicted static (mono.) displacement at H_{max} (in black). The fitting of equation (3) to each test is shown in grey. (c) Fitted $T_b(\zeta_b)$ function and (d) fitted $T_c(\zeta_c)$ function

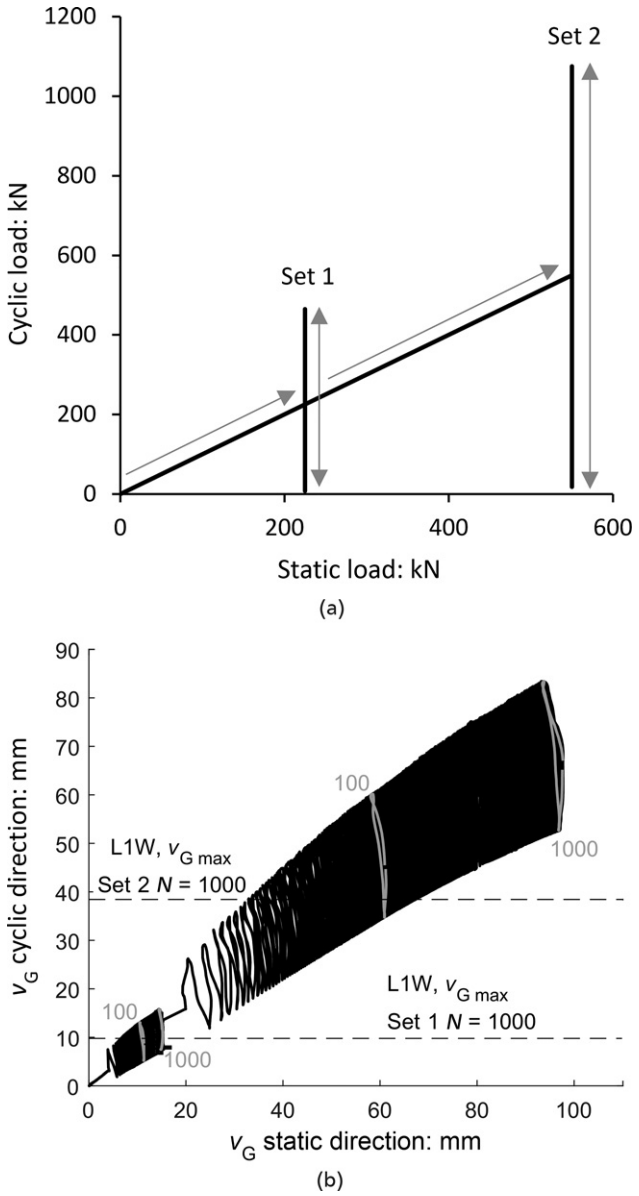

Fig. 13. Biaxial lateral cyclic test on LD14 (test 30): (a) illustration of load path and (b) plot of bi-directional lateral loading displacement response during test 30 on LD14 (layout shown in Fig. 2)

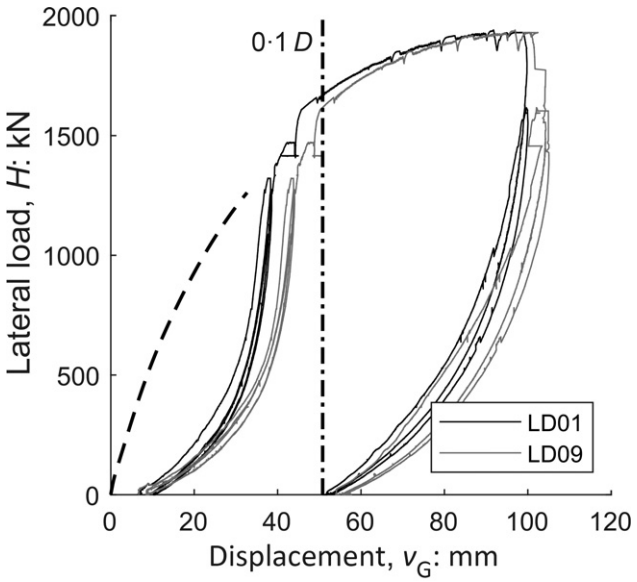

Fig. 14. Load–displacement behaviour for post uni-directional cyclic monotonic lateral test 24, with backbone curve from virgin monotonic test on LD11

The permanent accumulated cyclic displacement, $v_{G,acc}$, modelled using equations (3)–(5) is compared to the measured values in Fig. 11. The model captures most aspects of the field accumulation trends well, and generally predicts values within the bounds of the north and south test piles. However, the model performs less well for test 27, probably due to its slower initial loading rate.

Biaxial loading

Offshore piles often sustain biaxial cyclic loading when, for example, wind and wave directions differ. Fig. 13(a) shows the lateral biaxial loading scheme applied to pile LD14 to investigate the impact of conditions, such as a relatively steady fore–aft wind thrust acting in combination with periodic side–side wave excitation. Cyclic loading was applied while a perpendicular static load, H_{stat} was held steady in the other horizontal direction. Also shown are the resulting ground-level displacements generated in the static and cyclic loading directions. The pile tended to move predominantly in the resultant load direction, which in this case was biased towards the static loading axis. Lateral biaxial cycling led to more significant displacement accumulation (or ratcheting) than uniaxial, with v_G exceeding $D/10$ = 50·8 mm within 100 cycles on both axes. Displacement and gap growth was most marked over minimum loading stages of each cycle.

Post-cyclic monotonic axial tension tests

Gapping during cyclic lateral loading appears far more pronounced in the brittle chalk than in sands and clays (e.g. McAdam *et al.*, 2020). The damaging impact of cycling also appears to penetrate below the gaps and affect the lower pile sections that provide most axial shaft capacity. Monotonic ASTs (performed in the same way as the main axial loading programme) on piles LD01, LD04 and LD08, after completing all their lateral cycling, showed average shaft capacity losses of 56% compared to AST tests conducted on equivalent 'virgin' piles at the same ages (Jardine *et al.*, 2023).

Post-cyclic monotonic loading

Monotonic lateral loading checks were conducted as the final testing stage following the cyclic loading, displacing the piles at a nominal $D/300\,\text{min}^{-1}$ until their expected steel yield points were reached. With the exception of test 28, which had a single reloading loop, the post-cyclic monotonic tests involved three additional unload/reload loops employing the same displacement rate. The 'post uni-directional cycling' responses of LD01 and LD09 are illustrated in Fig. 14, which includes the backbone curve from the 'virgin monotonic test' on LD11. The large gaps formed during cyclic loading could only be closed after imposing displacements large enough to re-establish full contact between the chalk and the steel shaft. However, the cycling and gapping did not degrade the ultimate (v_G = $D/10$) monotonic lateral capacity or eventual load–displacement response, as noted in similar tests in clay and sand (Byrne *et al.*, 2020a; McAdam *et al.*, 2020). Table 4 summarises the final test's initial

stiffnesses and their permanent ground-level displacements after ultimate unloading. In all cases, the piles' initial load–displacement behaviour was significantly softer than under virgin monotonic loading, due principally to the cyclic gapping. The pile that experienced cyclic failure under lateral biaxial cyclic loading required the largest ground-level displacement of $v_G = D/4$ before re-establishing full contact.

CONCLUSIONS

This paper reports suites of monotonic and cyclic lateral load tests on highly instrumented 508 mm and 1220 mm dia. piles with L/D ratios between 6 and 20, driven at a well-characterised, low- to medium-density chalk site. The primary conclusions are listed below.

(*a*) The piles' lateral responses depended critically on their slenderness ratios. The $L/D = 20$ piles flexed during monotonic lateral loading and steel yielding occurred, even with relatively thick-walled piles, before ground-level displacements reached $D/10$. While local failure and cracking developed around the upper pile section, the displacements were largely recovered on unloading and the deeper pile sections indicated little evidence of permanent deformation.

(*b*) In contrast, $L/D = 6$ piles showed a softer monotonic load–displacement response, and much higher permanent displacements on unloading, as the piles underwent near-rigid body rotations and ultimate failure developed along most of the pile length. The $L/D = 6$ piles reached $v_G = D/10$ at approximately 30% lower head loads than those with $L/D = 20$.

(*c*) Lateral, p/D–v, reaction curves extracted from the field measurements and applied in 1D FE modelling reproduce well the monotonic response measured during tests on three pile diameters and length-to-diameter ratios at SNW. For full-scale application, the fitting of the soil reaction parameters would benefit from a PISA style calibration study given site-specific numerical analyses, with a numerical approach such as that set out by Pedone *et al.* (2023).

(*d*) Applying up to 2000 lateral one-way (uniaxial) load cycles to paired $L/D = 20$ piles led to accumulated displacements in the direction of loading. Calibrating the LeBlanc *et al.* (2010a) simplified cyclic accumulation model to these observations led to parameters comparable with established results in other materials and at different scales. This model reproduced the field trends well and, excluding one test, predicted values within the bounds of each test pile pair. The accumulated displacements were largely recovered on unloading. However, all piles developed clear gaps over their active and passive faces in line with the pile displacements that affected the piles' axial capacities negatively.

(*e*) Lateral biaxial cyclic loading deflected the piles in the direction of the resultant (monotonic) load and led to markedly larger cyclic and permanent displacements than equivalent one-way cycling.

(*f*) Soft post-cyclic monotonic behaviour persisted on monotonic reloading until the leading pile-to-chalk gap closed. High-amplitude lateral cycling also greatly reduced axial shaft capacities. Both features have significant implications when large-amplitude lateral cycles are expected at sites where chalk is encountered from the ground surface.

(*g*) The chalk's development of notably low p_{ult}/D values in comparison with laboratory test shear strengths is interpreted as being due to its highly brittle and pressure-dependent behaviour, as well as damage caused by pile driving. These features were examined in advanced numerical analyses performed under the parallel ALPHA research project, which offered a route for developing PISA-style design analyses for piles driven in similar chalks.

The experiment's reported and interpreted soil reaction curves represent a benchmark dataset for the calibration and validation of alternative numerical models and design approaches. New tests in different chalk grades and with varying pile geometries, under monotonic and cyclic loading conditions, will help extend the dataset and improve the scope for undertaking representative calibration and validation exercises.

ACKNOWLEDGEMENTS

The authors gratefully acknowledge support from the Engineering and Physical Science Research Council (EPSRC) grant EP/P033091/1, Royal Society Newton Advanced Fellowship NA160438 and Supergen ORE Hub 2018 (EPSRC EP/S000747/1). B. W. Byrne is supported by the Royal Academy of Engineering under the Research Chairs and Senior Research Fellowships scheme, while K. Vinck was supported by EPSRC grant EP/L016826/1, DEME and Imperial College. The provision of additional financial and technical support by the following project partners is also acknowledged gratefully: Atkins, Cathies, Equinor, Fugro, GCG, LEMS, Ørsted, Parkwind, RWE, Siemens-Gamesa, Scottish Power Renewables and Vattenfall. The authors also wish to acknowledge: Socotec UK Ltd as their main contractor for the field-testing programme and Marmota Engineering AG as the fibre-optic strain gauge specialists; Cambridge in situ for the pressuremeter tests; and Lankelma UK and Fugro Geoservices for in situ testing and rotary boreholes.

NOTATION

A	accumulated deformation pre-factor
b	accumulated deformation exponent
D	pile outer diameter
E	Young's modulus
G_{vh}	vertical component of shear modulus
H	lateral load
H_{cyc}	cycle lateral load amplitude
$H_{D/10}$	lateral load at $v_G = D/10$
$\bar{H}_{D/10}$	spline interpreted lateral load at $v_G = D/10$
H_{max}	maximum cycle lateral load
H_{mean}	mean cycle lateral load
H_{min}	minimum cycle lateral load
I	second moment of area
k_{init}	cycle initial stiffness
k_p	soil reaction curve initial subgrade modulus
k_{peak}	cycle peak stiffness
k_{sec}	cycle secant stiffness
L	pile length
M	internal bending moment
N	cycle number
n_p	soil reaction curve curvature parameter
p	distributed lateral soil reaction
p_u	ultimate lateral soil reaction
q_{max}	maximum deviatoric stress
q_t	corrected cone penetrometer tip pressure

T dimensionless cyclic load functions
t pile wall thickness
v lateral displacement
v_G lateral displacement at ground level
$v_{G,acc}$ accumulated lateral displacement at ground level
$v_{G,final}$ final lateral displacement at ground level
$v_{G,max}$ peak lateral displacement at ground level
$v_{G,s}$ ground level displacement predicted to occur on monotonic loading to H_{max}
$v_{G,0}$ displacement at start of cycling
v_u soil reaction curve ultimate displacement
z depth below ground level
α cyclic accumulation exponent
ε strain
ζ cyclic loading characteristic

REFERENCES

Ahmadi-Naghadeh, R., Liu, T. F., Vinck, K., Jardine, R. J., Kontoe, S., Byrne, B. & McAdam, R. A. (2022). A laboratory characterisation of the response of intact chalk to cyclic loading. *Géotechnique* **74**, No. 6, 527–539.

API (2014). *API RP 2A-WSD: recommended practice for planning, designing and constructing fixed offshore platforms – working stress design*, 22nd edn. Washington, DC, USA: American Petroleum Institute.

Beuckelaers, W. J. A. P. (2017). *Numerical modelling of laterally loaded piles for offshore wind turbines*. DPhil thesis, University of Oxford, Oxford, UK.

Bowden, A. J., Spink, T. W. & Mortimore, R. N. (2002). The engineering description of chalk: its strength, hardness and density. *Q. J. Engng Geol. Hydrogeol.* **35**, No. 4, 355–361.

Buckley, R. M., Jardine, R. J., Kontoe, S., Parker, D. & Schroeder, F. C. (2018). Ageing and cyclic behaviour of axially loaded piles driven in chalk. *Géotechnique* **68**, No. 2, 146–161.

Buckley, R. M., McAdam, R. A., Byrne, B. W., Doherty, J. P., Jardine, R. J., Kontoe, S. & Randolph, M. F. (2020). Optimization of impact pile driving using optical fibre Bragg grating measurements. *J. Geotech. Geoenviron. Engng – ASCE* **146**, No. 9, 1–15, https://doi.org/10.1061/(ASCE)GT.1943-5606.0002293.

Buckley, R. M., Jardine, R. J., Kontoe, S. J., Liu, T. F., Byrne, B. W., McAdam, R. A., Schranz, F. & Vinck, K. (2023). Axial cyclic loading of piles in low to medium density chalk. *Géotechnique* **74**, No. 6, 570–583, https://doi.org/10.1680/jgeot.22.00044.

Burd, H. J., Beuckelaers, W. J. A. P., Byrne, B. W., Gavin, K., Houlsby, G. T., Igoe, D., Jardine, R. J., Martin, C. M., McAdam, R. A., Muir Wood, A., Potts, D. M., Skov Gretlund, J., Taborda, D. M. G. & Zdravković, L. (2020a). New data analysis methods for instrumented medium scale monopile field tests. *Géotechnique* **70**, No. 11, 961–969.

Burd, H. J., Taborda, D. M. G., Zdravković, L., Abadie, C. N., Byrne, B. W., Houlsby, G. T., Gavin, K. G., Igoe, D. J. P., Jardine, R. J., Martin, C. M., McAdam, R. A., Pedro, A. M. G. & Potts, D. M. (2020b). PISA design model for monopiles for offshore wind turbines: application to a marine sand. *Géotechnique* **70**, No. 11, 1048–1066.

Byrne, B. W., McAdam, R. A., Burd, H. J., Houlsby, G. T., Martin, C. M., Beuckelaers, W. J. A. P., Zdravkovic, L., Taborda, D. M. G., Potts, D. M., Jardine, R. J., Ushev, E., Liu, T. F., Abadias, D., Gavin, K., Igoe, D., Doherty, P., Skov Gretlund, J., Pacheco Andrade, M., Muir Wood, A., Schroeder, F. C., Turner, S. & Plummer, M. (2017). PISA: new design methods for offshore wind turbine monopiles. In *Proceedings of 8th international conference offshore site investigation and geotechnics* (eds T. Powel), vol. 1, pp. 142–161. London, UK: SUT, https://doi.org/10.3723/OSIG17.142.

Byrne, B. W., McAdam, R. A., Burd, H. J., Beuckelaers, W. J. A.P., Gavin, K., Houlsby, G. T., Igoe, D., Jardine, R. J., Martin, C. M., Muir Wood, A., Potts, D. M., Skov Gretlund, J., Taborda, D. M. G. & Zdravković, L. (2020a). Monotonic lateral loaded pile testing in a stiff glacial clay till at Cowden. *Géotechnique* **70**, No. 11, 970–985.

Byrne, B. W., Houlsby, G. T., Burd, H. J., Gavin, K., Igoe, D., Jardine, R. J., Martin, C. M., McAdam, R. A., Potts, D. M., Taborda, D. M. G. & Zdravković, L. (2020b). PISA design model for monopiles for offshore wind turbines: Application to a stiff glacial clay till. *Géotechnique* **70**, No. 11, 1030–1047.

Ciavaglia, F., Carey, J. & Diambra, A. (2017). Monotonic and cyclic lateral tests on driven piles in Chalk. *Proc. Instn Civ. Engrs – Geotech. Engng* **170**, No. 4, 353–366.

Clayton, C. R. L., Matthews, M. C. & Heymann, G. (2003). The chalk. In *Characterisation and engineering properties of natural soils* (eds T. S. Tan, K. K. Phoon, D. W. Hight and S. Leroueil), pp. 1403–1434. Lisse, The Netherlands: Swets & Zeitlinger 1.

Jardine, R. J. & Potts, D. M. (1993). Magnus foundations: soil properties and predictions of field behaviour. In *Large-scale pile tests in clay*, pp. 69–83. London, UK: Thomas Telford Publishing.

Jardine, R. J., Kontoe, S., Liu, T. F., Vinck, K., Byrne, B. W., McAdam, R. A, Schranz F. Andolfsson, T. & Buckley, R. M. (2019). The ALPACA research project to improve design of piles driven in chalk. In *Proceedings of the 17th European conference on soil mechanics and geotechnical engineering*, p. 8. Reykjavik, Iceland: ECSMGE, doi: https://doi.org/10.32075/17ECSMGE-2019-71.

Jardine, R. J., Buckley, R. M., Liu, T., Andolfsson, T., Byrne, B. W., Kontoe, S., McAdam, R. A., Schranz, F. & Vinck, K. (2023). The axial behaviour of piles driven in chalk. *Géotechnique* **74**, No. 6, 553–569, https://doi.org/10.1680/jgeot.22.00041.

LeBlanc, C., Houlsby, G. T. & Byrne, B. W. (2010a). Response of stiff piles in sand to long-term cyclic lateral loading. *Géotechnique* **60**, No. 2, 79–90.

LeBlanc, C., Houlsby, G. T. & Byrne, B. W. (2010b). Response of stiff piles to random two-way lateral loading. *Géotechnique* **60**, No. 9, 715–721.

Liu, T. F., Ferreira, P. M. V., Vinck, K., Coop, M. R., Jardine, R. J. & Kontoe, S. (2022a). The behaviour of a low-to-medium density chalk under a wide range of pressure conditions. *Soils Found.* **63**, No. 1, 101268.

Liu, T. F., Ahmadi-Naghadeh, R., Vinck, K., Jardine, R. J., Kontoe, S., Buckley, R. M. & Byrne, B. (2022b). An experimental investigation into the behaviour of de-structured chalk under cyclic loading. *Géotechnique* **74**, No. 6, 540–552.

Lord, J. A., Clayton, C. R. L. & Mortimore, R. N. (2002). Report C574: Engineering in chalk. London, UK: Construction Industry Research and Information Association (CIRIA).

Lord, J. A. & Davies, J. A. G. (1979). Lateral loading and tension tests on a driven cased pile in chalk. In *Proceedings of the ICE conference on recent developments in the design and construction of piles* (ed A. M. Burt), pp. 113–120. London, UK: Institution of Civil Engineers.

Matthews, M. & Clayton, C. (2004). Large diameter plate tests on weathered in-situ chalk. *Q. J. Engng Geol. Hydrogeol.* **37**, No. 1, 61–72.

McAdam, R. A., Byrne, B. W., Houlsby, G. T., Beuckelaers, W. J. A. P., Burd, H. J., Gavin, K., Igoe, D., Jardine, R. J., Martin, C. M., Muir Wood, A., Potts, D. M., Skov Gretlund, J., Taborda, D., M. G. & Zdravković, L. (2020). Monotonic lateral loaded pile testing in a dense marine sand at Dunkirk. *Géotechnique* **70**, No. 11, 986–998.

Murff, J. D. & Hamilton, J. M. (1993). P-ultimate for undrained analysis of laterally loaded piles. *J. Geotech. Engng* **119**, No. 1, 91–107.

Pedone, G., Kontoe, S., Zdravkovic, L. & Jardine, R. J. (2020). Supergen ORE flexible funding research project ALPHA: Numerical analysis of laterally loaded piles driven in chalk. *Final Report*, Imperial College London, Sept. 2020.

Pedone, G., Kontoe, S., Zdravković, L., Jardine, R., Vinck, K. & Liu, T. (2023). Numerical modelling of laterally loaded piles driven in low-to-medium density fractured chalk. *Comput. Geotech.* **156**, 105252.

Pellew, A. L. (2002). *Field investigations into pile behaviour clay*. PhD thesis, Imperial College London, London, UK.

Pellew, A. & Jardine, R. J. (2008). *Aged steel displacement and bored concrete piles in London clay*. Bracknell, Berkshire, UK: IHS BRE Press.

Previtali, M., Ciantia, M. O. & Riccio, T. (2023). Numerical installation of OE piles in soft rocks within the GPFEM framework. In *Proceedings of the 10th European conference on numerical methods in geotechnical engineering*, p. 322. London, UK: International Society for Soil Mechanics and Geotechnical Engineering, doi: https://doi.org/10.53243/NUMGE2023-322.

Potts, D. M. & Zdravković, L. (2000). *Finite element analysis in geotechnical engineering: applications*. London, UK: Thomas Telford.

Richards, I. (2019). *Monopile foundations under complex cyclic lateral loading*. DPhil thesis, University of Oxford, Oxford, UK.

Schiffman, R. L., Chen, A. & Jordan, J. C. (1967). The consolidation of a half plane, MATE Report, 67-3, Chicago, IL, USA: U. Illinois.

Taborda, D. M. G., Zdravković, L., Potts, D. M., Burd, H. J., Byrne, B. W., Gavin, K. G., Houlsby, G. T., Jardine, R. J., Liu, T., Martin, C. M. & McAdam, R. A. (2020). Finite-element modelling of laterally loaded piles in a dense marine sand at Dunkirk. *Géotechnique* **70**, No. 11, 1014–1029.

Vinck, K., Liu, T. F., Jardine, R. J., Kontoe, S., Ahmadi-Naghadeh, R., Buckley, R. M., Byrne, B. W., Lawrence, J. A., Mcadam, R. A. & Schranz, F. (2022). Advanced in-situ and laboratory characterisation of the ALPACA chalk research site. *Géotechnique* **74**, No. 6, 512–526.

Wen, K. (2023). *Dynamic and monotonic axial loading responses of piles driven for offshore wind turbines*. PhD thesis, Department of civil and Environmental Engineering, Imperial College London, London, UK.

Wen, K., Kontoe, S., Jardine, R. J., Liu, T. & Pan, L. (2023). Non-linear finite-element analysis of axially loaded piles driven in chalk. In *Proceedings of 10th European conference on numerical methods in geotechnical engineering* (eds L. Zdravkovic, S. Kontoe, D. M. G. Taborda and A. Tsiampousi), p. 322. London, UK: International Society for Soil Mechanics and Geotechnical Engineering, doi: https://doi.org/10.53243/NUMGE2023-337.

Wen, K., Kontoe, S., Jardine, R. J. & Liu, T. (2024). Finite element modelling of pipe piles driven in low-to-medium density chalk under axial loading. *Comput. Geotech.* **172**, 106458.

Zdravković, L., Taborda, D. M. G., Potts, D. M., Abadias, D., Burd, H. J., Byrne, B. W., Gavin, K. G., Houlsby, G. T., Jardine, R. J., Martin, C. M., McAdam, R. A. & Ushev, E. (2020). Finite-element modelling of laterally loaded piles in a stiff glacial clay till at Cowden. *Géotechnique* **70**, No. 11, 999–1013.